CHAPTER 3

CFD MODEL AND OPTIMISATION METHODOLOGY

3.1 Basic equation, assumptions, and properties estimation

The simulations were carried out on a vertical hot-wall CVD reactor located at the DMSRDE (DRDO), Kanpur. The schematic diagram of the CVD reactor employed in this work is shown in Fig. 3.1. The reactor height is 1.4 m with a diameter of 0.5 m. Four inlets are provided at the base; three are located at the periphery, while one is positioned at the centre. The precursor gas mixture consisting of methane and hydrogen enters through these inlets and pyrolyses in the reactor. The PyC deposition occurs on multiple substrates, separated by 120 mm apart, and the diameter of each substrate plate is 0.3 m. They are placed on the rotating shaft at the centre of the reactor to ensure a uniform coating. The sufficient residence time of the reactants was achieved by placing the baffles at the reactor outlet. The reactor is non-axisymmetric; therefore, it is necessary to simulate the entire reactor volume.

Using twelve circumferential heating rods, the reactor wall was initially heated from ambient temperature (27^0C) to the appropriate temperature. It was then allowed to stabilise at the desired temperature. Four temperature sensors were strategically placed within the reactor to maintain temperature uniformity. Although the reactor hardware only allowed temperatures up to 1100^0C, simulations were run up to 2500^0C to find the limiting stage during deposition. When the temperature was reached, the CH_4 vapour was delivered into the reactor with the help of an H_2 and Ar mixture. Before entering the input nozzles, the whole gas flow rate was dispersed uniformly. The mixture's interaction with the buoyancy-driven flow resulted in cracking, which was followed by deposition on the substrate. The revolving shaft's centrifugal force disseminated the reactant towards the reactor wall, and maintaining an ideal rotation speed provided homogeneous deposition.

The amount of deposition was calculated by comparing the sample before and after the reaction. All tests used the same reaction time of 12 h. The reactor was purged with Ar after the reaction and allowed to cool to ambient temperature.

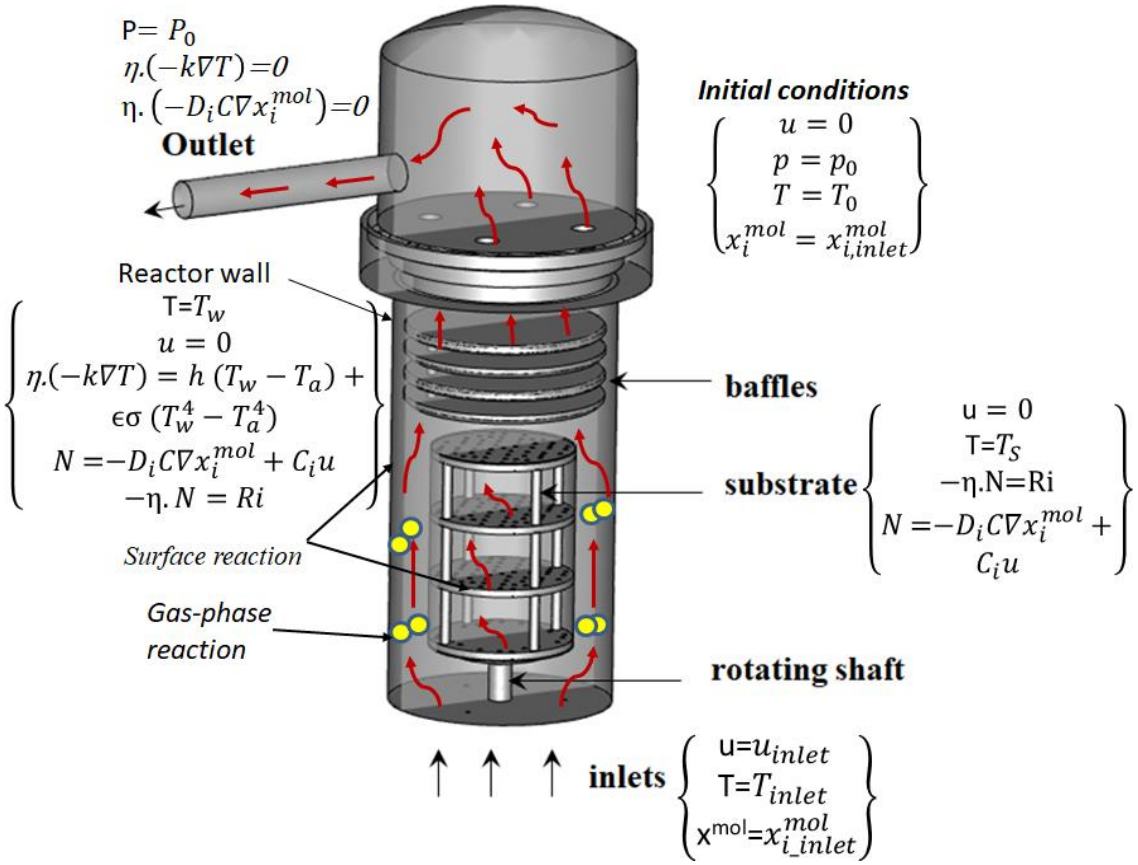

Fig. 3.1 The cross-sectional view of the commercial CVD reactor with boundary conditions used in the simulation

Several physical and chemical phenomena, such as mass, momentum, and heat transfer, along with chemical reactions, constitute the CVD process. These partial differential equations (PDEs) were numerically evaluated utilising the finite volume method assuming a continuum approach. As discussed in the subsequent section, the deposition process was simulated with well-defined gas and surface reaction kinetics. The equations governing the modelling of physical and chemical phenomena are expressed in the conservation of mass, momentum, energy, and species transport.

$$\frac{\partial \rho}{\partial t} + \nabla.\left(\rho\vec{u}\right) = 0 \tag{1}$$

$$\frac{\partial}{\partial t}\left(\rho\vec{u}\right) + \nabla.\left(\rho\vec{u}\vec{u}\right) = -\nabla P + \nabla.\tau + \rho\vec{g} + \vec{F}_B \tag{2}$$

Where $\tau = \mu\left[\nabla\vec{u} + \left(\nabla\vec{u}\right)^T - \frac{2}{3}\left(\nabla.\vec{u}\right)I\right]$ and

$$\frac{\partial}{\partial}\left(\rho x_i^{mol}\right)+\nabla.\left(\rho x_i^{mol}\vec{u}\right)=-\nabla.\vec{J}_i+M_i\sum_{i=1}^{N_r}\hat{R}_i^r \tag{3}$$

$$\frac{\partial}{\partial}\left(\rho h\right)+\nabla.\left(\rho h\vec{u}\right)=\nabla.\left[k_{eff}\nabla T-\sum_i h_i\vec{J}_i^h+\left(\tau.\vec{J}\right)\right] \tag{4}$$

The effect of thermal diffusion was taken into account in the species conservation equation. Due to this effect, large molecules diffuse less rapidly towards the heated surface compared to small ones. The combined flux due to molecular and thermal diffusion of species *i*, is presented as:

$$J_i=-\frac{\rho D_i^m}{M_i}\nabla x_i^{wt}-D_i^T\frac{\nabla T}{T} \tag{5}$$

The transport properties such as viscosity, diffusivity, and thermal conductivity of the gas mixture were estimated using the kinetic theory of gases. The mixture enthalpy was calculated as

$$h_i=h_i^0+\int_{T_{ref}}^{T}C_p dT \tag{6}$$

The specific heat capacity of species, *i*, at constant pressure was expressed in the NASA polynomials. The coefficients of these polynomials were obtained from the literature (Reinisch et al., 2011). The mass diffusivity for species, *i*, in the mixture D_i^m was estimated using Eq. (7).

$$D_i^m=\frac{1-x_i^{mol}}{\sum_{j,j\neq i}x_j^{mol}/D_{ij}^m} \tag{7}$$

The thermal diffusivity was estimated using the empirical expression given by Eq. (8) (Kuo et al., 2005).

$$D_i^T=-2.59\times10^{-7}T^{0.659}\left(\frac{M_i^{0.511}x_i^{mol}}{\sum_{i=1}M_i^{0.511}x_i^{mol}}-x_i^{wt}\right)\left(\frac{\sum_{i=1}M_i^{0.511}x_i^{mol}}{\sum_{i=1}M_i^{0.489}x_i^{mol}}\right) \tag{8}$$

The average rate of deposition (RD) and uniformity index (UI) was calculated as:

$$\overline{RD}=\frac{\int RD dA}{A} \tag{9}$$

$$UI=\frac{\int|\mathrm{RD}-\overline{RD}|\,dA}{A} \tag{10}$$

where A is the total area of the substrate.

3.2 Gas and surface reaction models

A detailed gas-phase kinetic modelling for light hydrocarbon pyrolysis in the CVD reactor was accomplished by many researchers. Norinaga et al. reported a kinetic study of PyC deposition from various precursors (Norinaga et al., 2006). They proposed a lumped parameter model with the assumption that PyC deposits directly from ethylene and acetylene. Later, a qualitative model was developed by Descamps et al. for propane pyrolysis and explained kinetic and microstructure transitions using two parallel reaction pathways (Descamps et al., 2001). These models provided a good foundation for further investigation. However, the limitation of these models is that they work in a narrow operating parameter window and do not render a fundamental understanding of the process. Consequently, a comprehensive gas-phase reaction mechanism with hundreds of elementary steps has been proposed. Recently, Hu et al. presented a model that consists of 241 species and 909 reactions for CH_4 pyrolysis, which predicts mole fractions of dominant species without adjusting kinetic parameters (Hu et al., 2016). However, solving a large number of CFD solver reactions is computationally expensive and not possible in many cases. Therefore, a reduced reaction mechanism was developed by Birakayala et al (Birakayala and Evans, 2002). Though this model is often used to depict the gas phase CH_4 pyrolysis, it underestimates the mole fractions of the dominant species in the present case. Our research group recently modelled the gas phase of CH_4 pyrolysis, and a relatively small model with 13 species and 29 reactions was proposed for CH_4 pyrolysis (Shinde and Pradeep, 2021). It was found that this model is more accurate compared to the models reported earlier in the literature. The reduced model used in the present study is given in Table 3.1 (Shinde and Pradeep, 2021).

Compared to the gas phase, the surface reaction mechanism is more complex due to the dynamic events on the depositing surface. Several speculative theories that have assumed the immediate decomposition of adsorbed species have been proposed to describe the PyC formation (Benzinger et al., 1996). The pre-exponential factor and apparent activation energy were estimated by assuming the whole process as the first-order reaction. However, precise knowledge of the rate-limiting step is still missing in the literature (Yu et al., 2016a). The boundary layer diffusion, nucleation, and crystal growth make understanding the surface reactions more complex (Ali and Ürgen, 2017, 2011b). It has been concluded that the concentration of intermediates depends on the identity of the carbon precursor, its initial mole fraction, flow rate, residence time, and temperature (Hu and Hüttinger, 2001). Dong et al.

modelled the multi-step reactions and correlated the formation of a distinct PyC structure considering C_2H_2, C_2H_4, and C_6H_6 as dominating growth species (Dong and Hüttinger, 2002). They investigated hydrogen inhibition on the carbon deposition for the mixture of CH_4/H_2, and the rate constants of the surface reaction were obtained by fitting the experimental results. The surface reaction model developed by Li et al. was adopted in the present study and given in Table 3.1 (Li et al., 2008). The surface site density was evaluated to be 6.3102×10^{-8} kmol/m^2 from geometrical considerations (Lacroix et al., 2010), and PyC bulk density was assumed to be 2.20 g/cm^3.

Table 3.1 Gas-phase and surface reactions along with kinetic parameters of methane pyrolysis (Norinaga et al., 2006; Shinde and Pradeep, 2021).

No.	Reaction	A	β_T	E (kJ/mol)
Gas-phase reactions				
G1	$C_2H_4 \leftrightarrow C_2H_3 + H$	3.98×10^{17}	0.0	410.86
G2	$H + C_2H_4 \leftrightarrow C_2H_3 + H_2$	1.32×10^{06}	2.5	46.86
G3	$H + H \leftrightarrow H_2$	1.00×10^{00}	0.0	0.0
G4	$CH_4 \leftrightarrow H + CH_3$	1.00×10^{17}	0.0	358.98
G5	$CH_3 + C_2H_4 \leftrightarrow C_2H_3 + CH_4$	5.00×10^{12}	0.0	54.39
G6	$CH_3 + H_2 \leftrightarrow CH_4 + H$	2.75×10^{04}	2.5	39.32
G7	$2CH_3 \leftrightarrow C_2H_6$	3.18×10^{41}	-7.0	11.29
G8	$CH_3 + CH_4 \leftrightarrow C_2H_6 + H$	8.00×10^{13}	2.0	167.36
G9	$C_2H_5 \leftrightarrow C_2H_4 + H$	2.04×10^{15}	0.0	31.0
G10	$C_2H_6 \leftrightarrow C_2H_5 + H$	2.08×10^{38}	-7.1	129.7
G11	$2CH_3 \leftrightarrow C_2H_5 + H$	3.01×10^{13}	0.0	56.48
G12	$CH_3 + CH_4 \leftrightarrow C_2H_5 + H_2$	1.00×10^{13}	0.0	96.23
G13	$C_2H_5 + H \leftrightarrow C_2H_4 + H_2$	2.00×10^{12}	0.0	0.0
G14	$2C_2H_4 \leftrightarrow C_2H_5 + C_2H_3$	1.82×10^{14}	0.0	269.86
G15	$C_2H_6 + C_2H_3 \leftrightarrow C_2H_5 + C_2H_4$	1.08×10^{-03}	4.5	14.64
G16	$C_2H_6 + H \leftrightarrow C_2H_5 + H_2$	5.40×10^{02}	3.5	21.75
G17	$CH_3 + C_2H_6 \leftrightarrow CH_4 + C_2H_5$	5.50×10^{-01}	4.0	37.65
G18	$C_3H_6 + H \leftrightarrow C_2H_4 + CH_3$	3.40×10^{13}	0.0	14.64
G19	$C_3H_6 \leftrightarrow C_2H_3 + CH_3$	2.50×10^{14}	0.0	368.19

G20	$C_3H_6 + C_2H_3 \leftrightarrow C_4H_6 + CH_3$	1.00×10^{00}	0.0	0.0
G21	$C_4H_6 \leftrightarrow 2C_2H_3$	4.07×10^{16}	0.0	390.78
G22	$C_4H_6 + C_2H_3 \leftrightarrow C_6H_6 + H + H_2$	3.98×10^{10}	0.0	0.0
G23	$C_4H_6 + H \leftrightarrow C_2H_4 + C_2H_3$	5.01×10^{11}	0.0	0.0
G24	$C_2H_4 \leftrightarrow C_2H_2 + H_2$	8.00×10^{12}	0.4	371.12
G25	$C_2H_3 + H \leftrightarrow C_2H_2 + H_2$	3.00×10^{13}	0.0	0.0
G26	$C_3H_6 \leftrightarrow C_2H_2 + CH_4$	1.80×10^{12}	0.0	292.88
G27	$C_2H_3 \leftrightarrow C_2H_2 + H$	7.94×10^{14}	0.0	129.70
G28	$C_4H_6 + H \leftrightarrow C_2H_3 + C_2H_2 + H_2$	3.16×10^{14}	0.0	60.66
G29	$C_4H_6 \leftrightarrow C_2H_2 + C_2H_4$	8.40×10^{14}	0.0	355.64
Surface reactions				
S1	$C_2H_4 \rightarrow 2C(s) + 2H_2$	7.24×10^{01}	0.0	154.39
S2	$C_2H_2 \rightarrow 2C(s) + H_2$	1.35×10^{01}	0.0	125.52
S3	$C_6H_6 \rightarrow 6C(s) + 3H_2$	4.71×10^{05}	0.0	215.89

3.3 Boundary condition and solution procedure

The following assumptions were made to solve the above-mentioned governing equations: the flow was assumed to be a continuum, laminar, and ideal compressible gas. No-slip, impermeable boundary conditions were imposed on the solid surfaces, and zero species gradients were employed in the case of non-reacting walls. The reactor outlet flow was supposed to be fully developed. The thermal radiation effects are neglected because the reactor is operated at low pressure (50-500 mbar). It has been observed that the absorption coefficients of light hydrocarbons are very low under such operating pressure. In addition, the temperature inside the reactor is almost homogeneous. Therefore, the absorption of thermal radiation was ignored in the present work (Minakov et al., 2019). However, the heat loss due to radiation is accounted for in the boundary condition. The various operating conditions employed in the simulation are depicted in Fig. 3.1.

Table 3.2 The range of operating parameters used in the CFD simulation.

Parameter	**Value**	**Unit**
Reactor temperature	900-1100	^{0}C
Operating Pressure	100-1000	mbar
Speed of rotation	1	rpm

Inlet mole CH_4	0.2-1	--
Inlet mole H_2	0-0.8	--
Inlet mole C_2H_4 and C_2H_2	0	--
Total flow rate	10-30	lpm
Inlet gas temperature	80	^0C

Fig. 3.2 Schematic representation of unstructured tetrahedral mesh used for the computational domain

The reactor geometry was built in Ansys SpaceClaim, and the meshing was done using the ANSYS Workbench mesh generator. The high-quality unstructured tetrahedral mesh (skewness < 0.7) was used for the computational domain as depicted in Fig. 3.2. ANSYS Fluent, a commercial package, was used to perform simulations. The grid independence study was conducted by systematically increasing the number of elements from 2,012,374 to

2,952,435. Several key variables, including velocity, temperature, C_2H_2 concentration, and deposition rate, were closely monitored to assess convergence. The convergence of these variables was evaluated at various critical points within the domain, including near the inlet, outlet, and regions with high gradients, to ensure an accurate representation of the flow field. Steady-state numerical simulations were performed on various grid sets under identical boundary conditions. The resulting inlet Reynolds number was compared, revealing a continuous increase with the grid number up to 3.5 million, as shown in Fig. 3.3. Beyond this point, the Reynolds number stabilized. Considering available computational resources, a grid number of 3,660,910 million was selected for subsequent simulations where the relative increase of less than 1% in the cell values of the aforementioned variables

The simulations were conducted using Ansys, a commercial finite volume element software. Numerical grids with quadrilateral elements were generated based on the reactor geometry, resulting in a total mesh of 3,660,910 elements for this study. The convective-diffusive transport equations were discretized using a second-order upwind scheme. The discretized equations, along with the boundary conditions, were solved using the pressure-based COUPLED algorithm. The time step was taken to be 0.001 s for all the simulations. Appropriate relaxation factors were applied to pressure, velocity, temperature, and concentration to ensure a stable solution. Convergence was achieved when the residuals in the governing equations were less than 10^{-3}. The time step for all simulations was set to 0.001 seconds. A grid independence study was also performed by varying the number of elements from 1,012,374 to 4,952,435. It was observed that the relative increase in the cell Reynolds number was less than 1% after 3,660,910 elements, confirming the adequacy of the chosen grid size. The following points summarize the approach and criteria used to ensure computational convergence in our study: i) Residual Monitoring: The residuals of the governing equations (continuity, momentum, energy, and species transport) were closely monitored. Convergence was deemed achieved when all residuals fell below 10^{-3}. ii) Key Variable Monitoring: Specific variables such as velocity, temperature, C_2H_2 concentration, and deposition rate were tracked to ensure they reached steady-state values. iii) Mass and Energy Conservation: The overall mass and energy entering and leaving the system were checked to ensure they balanced within an acceptable tolerance, preventing unphysical accumulation or depletion. By adhering to these criteria, we ensured the accuracy and reliability of our computational results.

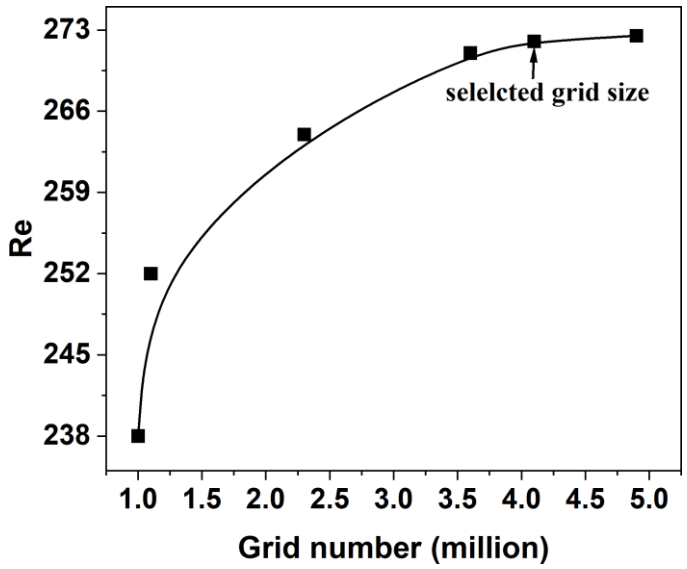

Fig. 3.3 Grid independence test.

3.3 Machine learning model for prediction of PyC deposition

A support vector machine (SVM) algorithm was employed to envisage how process variables such as temperature, pressure, inlet flow rate, and concentration of CH_4 affect the PyC deposition and film uniformity. Thus, there are two dependent variables: deposition rate and film uniformity, while four parameters, including reaction temperature, pressure, the concentration of CH_4, and total flow rate, are used as independent variables. Before training the models, the data were scaled using Eq. (11) to reduce multi-collinearity produced by higher-order terms.

$$x_i^{scaled} = \frac{x_i - \min(x_n)}{\max(x_n)} \tag{11}$$

10-fold cross-validation was availed to optimise the model hyperparameter so that the problems of overfitting and selection bias are minimised. One round of cross-validation was performed by dividing the data into complementary subsets, training the model on one subset, and validating on the other. In this way, several rounds of cross-validations were performed to reduce the variability of the model prediction on new data. The advantage of this procedure compared to the repeated random sub-sampling is that all sample data points are used to train and validate the model, and each data point is used only once for verification.

The SVM, a robust classifier, was used to correlate various process parameters with deposition rate and film uniformity. Support Vector Regression (SVR) is an SVM extension when applied to regression (Chen, 2007). There are many variants of SVR; however, ε-

insensitive regression was implemented in this study. The goal of SVR is not to minimise the error but to ensure it is within an acceptable range and to find an appropriate line (or hyperplane in higher dimensions) that fits the data. For n predictors, the hyperplane consists of n-1 dimensions. The best-fit line is the hyperplane with the maximum number of data points within a distance, sometimes referred to as the margin. Data points with residuals outside the margin contribute to the regression fit and support vectors. SVR achieves the fit by minimising the L2-norm of the coefficient vector while constraining the absolute error within a specified range. The solution to the SVR is reduced to the following optimisation problem (Hwang et al., 2021a).

$$\min \frac{1}{2}||\omega||^2 + C\sum_{k=1}^{n}|\xi_k| \tag{12}$$

Subject to $|y_k - \langle \omega_k, x_k \rangle - b| \leq \varepsilon + |\xi_k|$ (13)

Where ω_k is the coefficient of the model, and x_k and y_k are predictor and response, respectively, and C is a hyperparameter used to penalise large residuals. The value of C was obtained by trial and error (called grid search) over a grid of possible values such that the best value corresponds to the minimum training error. The term $\langle \omega_k, x_k \rangle$ in Eq. (13) denotes the dot product of the two elements w_k and x_k, which was replaced with a Gaussian kernel function while fitting the model. ε is the acceptable margin of error on both sides of the fitted line and the deviation of each data point from the line. The above formulation is based on the assumption that the corresponding convex optimisation problem is feasible. The performance of the model was estimated concerning the correlation coefficient (R^2), root means square error (RMSE) and means absolute error (MAE).

$$R^2 = 1 - \frac{\sum_{k=1}^{n}(y_k - \hat{y}_k)^2}{\sum_{i=1}^{n}(y_k - \bar{y})^2} \tag{14}$$

$$MAE = \sum_{k=1}^{n}\frac{|\hat{y}_k - y_k|}{n} \tag{15}$$

$$RMSE = \sqrt{\frac{\sum_{k=1}^{n}(\hat{y}_k - y_k)^2}{n}} \tag{16}$$

The variables $\bar{y}$, $\hat{y}_k$, y imply the mean, estimated, and observed values of the deposition rate (y1) and uniformity index (y_2), respectively.

3.4 Nelder-Mead algorithm

The Nelder-Mead algorithm, also known as the downhill simplex method, is a multidimensional optimisation process used to find the minimum of an objective function. It is a direct search or derivative-free optimisation approach developed by John Nelder and Roger Mead. It is a heuristic technique to minimise a function using a dynamic simplex (Shevkunov et al., 2019). It considers (n+1) points on the n-dimensional space and ensures better convergence by adjusting the step size based on the loss function. Suppose a new point is better than the previous one in subsequent iterations, the step size increases (expansion) to move to the minima faster. Otherwise, the step size is reduced (contraction) to converge around the minima. The function fitted previously using an SVM algorithm was evaluated at those n+1 points and used to find the optimal condition for the CVD reactor. The methodology framework employed in optimising the CVD reactor is illustrated in Fig. 3.4. x_B, x_w, and x_G in Fig. 3.4 represents the best, worst and good points. The new points required to locate the optimal value can be estimated as $x_M = \frac{x_B + x_G}{2}, x_R = 2x_M - x_W \quad x_{C_1} = \frac{x_R + x_M}{2}, x_{C_2} = \frac{x_W + x_M}{2}$. Detailed steps involved in the NM algorithm can be found elsewhere (Shevkunov et al., 2019).

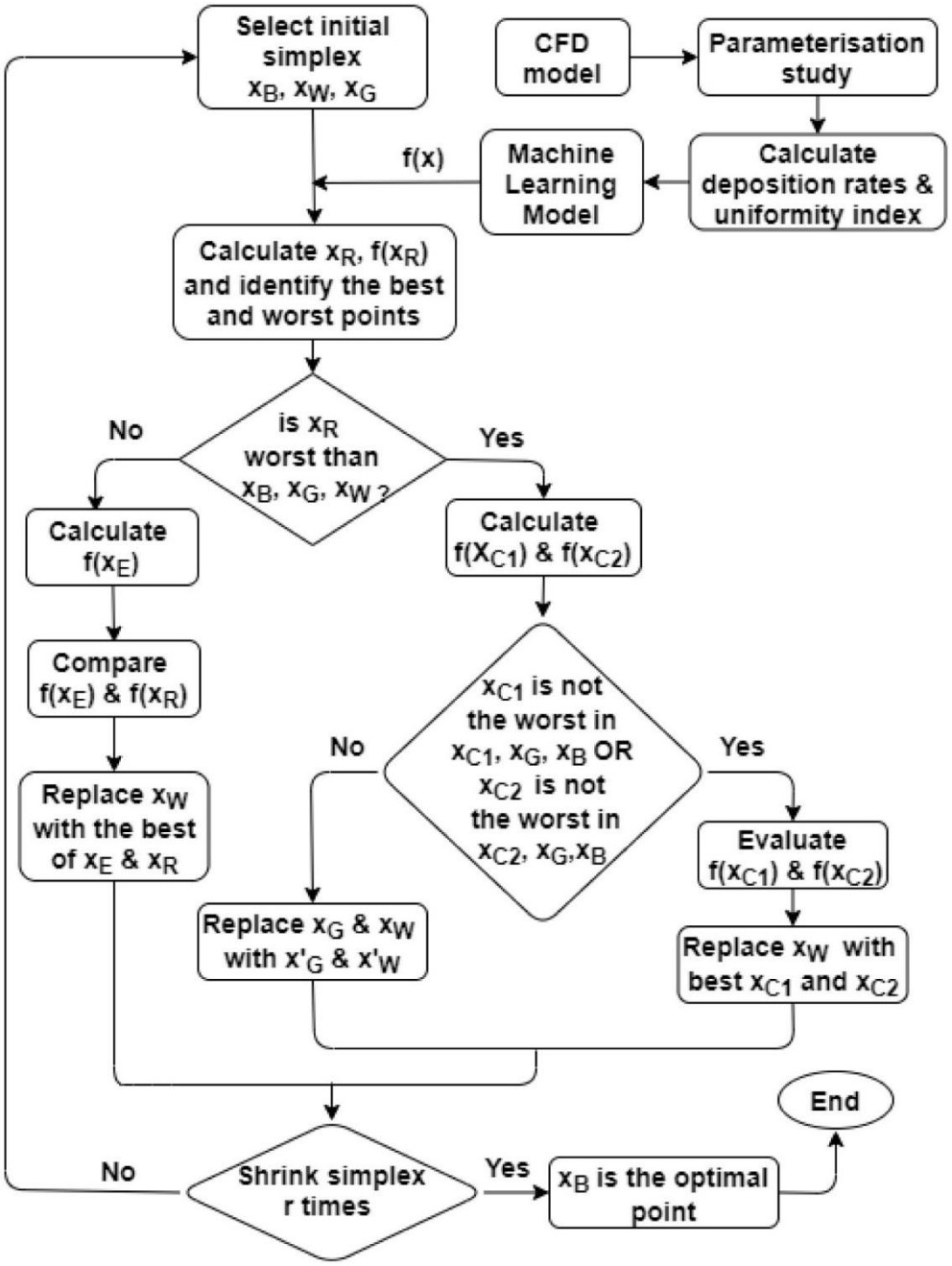

Fig. 3.4 Methodology framework for the optimisation of CVD reactor with the Nelder-Mead algorithm.

Steps involved in the NM algorithm:

1. **Initialization:**
   - Start with a simplex, which is a set of n+1 points in n-dimensional space.
   - Evaluate the objective function at each vertex of the simplex.
2. **Ordering:**

- Order the vertices based on the function values, so the best vertex has the lowest function value, and the worst has the highest.

3. **Reflection:**
   - Reflect the worst point across the centroid of the remaining points.

4. **Expansion, Contraction, or Reduction:**
   - If the reflected point is better than the second-worst, consider expanding farther in that direction.
   - If the reflected point is the new best, try expanding even more.
   - Contract towards the centroid if the reflected point is worse than the second-worst.
   - If the worst point remains the worst after reflection, contract the whole simplex towards the best point.

5. **Termination:**
   - Repeat the process until convergence criteria are met (e.g., a certain level of accuracy is achieved, or a maximum number of iterations is reached).

3.6 Objective function

After fitting the ML model, the function y (as given in Eq. (17)), which combined the PyC deposition and the film uniformity, was maximised by minimising -y. The NM algorithm was used for locating the optimal combination of the process variables. The optimisation algorithm was initialised using randomly selected data points to avoid the problem of local minima. Constraints were imposed on the response variables to avoid searching for values beyond the observation space. Finally, optimisation was performed on the functions fitted using the SVR. The optimisation problem can be stated as follows:

Maximise $y = \alpha \times y_1 + \beta \times y_2$

Where $y = \begin{cases} 0 \ if \ \ \mathrm{y}_1 \geq y_1^{upper} \\ \mathrm{y} \ if \ \ \mathrm{y}_1 < y_1^{upper} \end{cases}$

Subject to:

$900^0 C \leq T \leq 1100^0 C$

$$50\ mbar \le P \le 1000\ mbar \qquad (17)$$
$$10\ \text{slm} \le Q \le 30\ \text{slm}$$
$$0.2 \le mol.frac \le 1$$

Where $y_i(i)$ represents the function evaluated at i[th] iteration. The goal is to simultaneously maximise the average deposition rate (y_1) and the uniformity index (y_2). Besides, searching the acceptable range of each process parameter given in Eq. (17), the average growth rate was restricted to be lower than the upper limit value ($y_1^{upper} = 357 \times 10^{-9}\,\text{kg/m}^2\text{s}$). Our experience suggests thicker film (y_1^{upper}) creates high intrinsic stress and produces cracks or delaminates at elevated temperatures. Therefore, the upper limit for deposition rate was restricted below this value for obtaining an optimal solution. The step-by-step procedure followed for the optimisation of the CVD reactor is described below as:

Step 1: Set the acceptable range of each process parameter (independent variables) and initialise the simplex.
Step 2: Estimate the objective function given in Eq. (17).
Step 3: Perform various actions, including ordering, expansion, contraction, reflection and shrink, to search for the optimal value.
Step 4: Set the obtained values and evaluate the performance of the objective function.
Step 5: Check the convergence criteria. If the termination criterion is satisfied, then end the loop or else return to step 1

References

1. Ali, M., Ürgen, M., 2017. Switching dynamics of morphology-structure in chemically deposited carbon films - a new insight. Carbon. 122, 653-663. https://doi.org/10.1016/j.carbon.2017.07.021
2. Benzinger, W., Becker, A., Hüttinger, K. J., 1996. Chemistry and kinetics of chemical vapour deposition of pyrocarbon: I. fundamentals of kinetics and chemical reaction engineering. Carbon. 34, 957–966. https://doi.org/10.1016/0008-6223(96)00010-3
3. Birakayala, N., Evans, E. A., 2002. A reduced reaction model for carbon CVD/CVI processes. Carbon. 40, 675-683. https://doi.org/10.1016/S0008-6223(01)00184-1

4. Chen, K. Y., 2007. Forecasting systems reliability based on support vector regression with genetic algorithms. Reliab. Eng. Syst. 92, 423-432. https://doi.org/10.1016/j.ress.2005.12.014

5. Deivendran, B., Shinde, V. M., Kumar, H., Prasad, N. E. 2021. 3D modelling and optimisation of sic deposition from CH_3SiCl_3/H_2 in a commercial hot-wall reactor. J. Cryst. Growth. 554, 125944. https://doi.org/10.1016/j.jcrysgro.2020.125944

6. Descamps, C., Vignoles, G. L., Féron, O., Langlais, F., Lavenac, J., 2001. Correlation between homogeneous propane pyrolysis and pyrocarbon deposition. J. Electrochem. Soc. 148, 695-708.

7. Dong, G. L., and Hüttinger, K. J., 2002. Consideration of reaction mechanisms leading to pyrolytic carbon of different textures. Carbon. 40, 2515–2528. https://doi.org/10.1149/1.1402981

8. Hu, C., Li, H., Zhang, S., Li, W., 2016. A molecular-level analysis of gas-phase reactions in chemical vapour deposition of carbon from methane using a detailed kinetic model. J. Mater. Sci., 51, 3897-3906. https://doi.org/10.1007/s10853-015-9709-2

9. Hu, Z., Hüttinger, K. J., 2001. Chemistry and kinetics of chemical vapour deposition of pyrocarbon: VIII. carbon deposition from methane at low pressures. Carbon. 39, 433-441. https://doi.org/10.1016/S0008-6223(00)00143-3

10. Hwang, G., Kim, T., Shin, J., Shin, N., Hwang, S., 2021. Machine learnings for CVD graphene analysis: from measurement to simulation of SEM images. J. Ind. Eng. Chem. 101, 430-444. https://doi.org/10.1016/j.jiec.2021.05.031

11. Kuo, K. K., 1986. Principles of Combustion. John Wiley and Sons, New York.

12. Li, A., Norinaga, K., Zhang, W., Deutschmann, O., 2008. Modeling and simulation of materials synthesis: chemical vapour deposition and infiltration of pyrolytic carbon. Compos. Sci. Technol. 68, 1097-1104. https://doi.org/10.1016/j.compscitech.2007.07.007

13. Li, A., Norinaga, K., Zhang, W., Deutschmann, O., 2008. Modelling and simulation of materials synthesis: chemical vapour deposition and infiltration of pyrolytic carbon. Compos. Sci. Technol. 68, 1097-1104. https://doi.org/10.1016/j.compscitech.2007.07.007

14. Minakov, A. V., Simunin, M. M., Ryzhkov, I. I., 2019. Modelling of ethanol pyrolysis in a commercial CVD reactor for growing carbon layers on alumina substrates. Int. J. Heat Mass Transfer.145, 118764. https://doi.org/10.1016/j.ijheatmasstransfer.2019.118764

15. Reinisch, G., Vignoles, G. L., Leyssale, J.-M., 2011. Reaction mechanism for the thermal decomposition of $BCl_3/CH_4/H_2$ gas mixtures. J. Phys. Chem. A. 115, 11579-11588. https://doi.org/10.1021/jp2039114

16. Shevkunov, N. O., Zhigunova, A. v., Shevkunova, A. V., 2019. Modelling parameters of the production project. IOP Conf. Ser. Mater. Sci. Eng. 560, 012043. https://doi.org/10.1088/1757-899X/560/1/012043

17. Shinde, V. M., Pradeep, P., 2021. Detailed gas-phase kinetics and reduced reaction mechanism for methane pyrolysis involved in CVD/CVI processes. J. Anal. Appl. Pyrol. 154, 104998. https://doi.org/10.1016/j.jaap.2020.104998

18. Yu, K., Hayman, C. C., Manjunath, S., Fan, W., Martin, I. T., Martin, H. B., Sankaran, R. M., 2016. A combined CFD modelling and experimental study of pyrolytic carbon deposition, Diamond Relat. Mater. 70, 173-178. https://doi.org/10.1016/j.diamond.2016.10.010